RSC Advances

PAPER

View Article Online
View Journal | View Issue

Cite this: *RSC Adv.*, 2022, **12**, 17012

Improved performance of self-reactivated Pt–ThO_2/C catalysts in a direct ethanol fuel cell

Yubing Xue, [a] Dashu Pan,[a] Feng Zuo,[b] Songtao Xiao,[a] Xiang Li,[a] Fuyan Lou,[a] Mingming Li[a] and Yinggen Ouyang*[a]

A novel self-reactivated catalyst Pt–ThO_2/C was prepared for the first time by selecting radioactive material ThO_2 as the catalytic additive to address the low activity and toxicity of the anode Pt/C catalyst in a direct ethanol fuel cell. The catalytic activity and resistance to CO poisoning of Pt-6.67 wt%ThO_2/C were found to be superior to those of Pt/C–$NaBH_4$ in electrochemical workstation and single-cell tests. It is speculated that the exist of ThO_2 not only improves the catalytic activity *via* the synergistic effect of Pt and Th, but also produces a large amount of radiolysis products, OH radicals, due to ^{232}Th which oxidatively desorbs CO from Pt–CO_{ads} and solves the CO poisoning problem.

Received 14th April 2022
Accepted 1st June 2022

DOI: 10.1039/d2ra02398a

rsc.li/rsc-advances

Introduction

According to the 2016–2021 China New Energy Industry Development Prospects and Investment Strategic Planning Analysis Report, it is well established that of the proven fossil fuels all over the world, coal could be exploited for 110 years, oil for 53 years and natural gas for 54 years, while burning fossil fuels would cause the emission of 32 billion tonnes of carbon dioxide, 120 million tonnes of sulphur oxides and 100 million tonnes of nitrogen oxides in the next single year. The shortage of fossil fuels and the environmental pollution caused by combustion for power generation are becoming salient. Consequently, there is an urgent need to explore renewable and clean alternative energy sources as well as to develop new power generation technologies to avoid combustion for power generation.[1,2] The direct alcohol fuel cell (DAFC), an energy conversion device with compact configuration and convenient operation, can convert the chemical energy of alcohols such as ethanol,[3] methanol,[4] ethylene glycol,[5] propanol[6] and butanol[7] directly into electricity in an environmentally friendly way, *i.e.*, the combustion products do not contain sulphur oxides or nitrogen oxides which are noxious to the environment and human health.[8,9] The DAFC systems have been utilized in vehicles and especially portable electronic devices like laptops, mobile phones and power packs due to the high energy density of alcohol, convenience, durability, and stable power supply.[10–13] Direct ethanol fuel cells (DEFCs) are DAFCs using ethanol as the fuel with higher energy density and less toxic intermediate products compared to methanol.[14]

Numerous fundamental studies have been reported that Pt-based catalyst shows the most excellent performance in acidic DEFCs[15] and Nafion membranes, the proton exchange membrane (PEM) are commonly applied.[16–19] What's more, the design of multimodal porous carbon for the interfacial microporous layer has also been studied to improve the performance of electrocatalyst.[20,21] The development of electrocatalysts plays a crucial role in improving the performance of fuel cells. In addition to exploring high-efficient approaches to synthesize catalysts,[22] the factors responsible for superior catalytic activity and stability of nanocatalysts have also been inspected to further conduct the synthesis of electrocatalysts.[23] And the impacts of ligands on the catalytic activities of like PtRu, PtPd and Pt/C have deepen the understanding of the application of heterogeneous catalysis.[24]

However, fabrication or manufacture of Pt/C catalyst is the foremost obstacle to the application and commercialization of DEFC because of its high cost (accounts for 36% of the fuel cell's total expenditure) and the performance drop attributed by the poor ability to resist CO poisoning.[15,25,26] Ethanol in the anode catalytic layer generates CO-intermediates as a result of incomplete oxidation.[27] It has been confirmed by *in situ* infrared spectroscopy that the intermediate product CO is adsorbed on the Pt surface by linear adsorption, forming stable Pt carbonyl groups (Pt + CO → Pt–CO_{ads}). As CO covers the active site of Pt, it affects the Pt/C catalytic performance and prevents further dissociation of ethanol, ultimately leading to a dramatic decrease in the overall cell performance.[28–31]

In addition to scan the poisoned Pt/C electrode in 0.5 mol L^{-1} H_2SO_4 solution, there are three other ways to settle the catalyst performance drop caused by the CO poisoning: (1) based on the bifunctional mechanism, the addition of some non-Pt elements to the Pt/C catalyst can contribute to the removal of CO. M. Watanabe *et al.* explained the detoxification

[a]*China Institute of Atomic Energy, Beijing, 102413, China. E-mail: yubing_xue@163.com*

[b]*School of Nuclear Science and Technology, Xi'an Jiaotong University, Xi'an, 710049, China*

mechanism of Pt–Ru/C catalysts, where Pt adsorbs the intermediate product CO to form Pt carbonyl groups ($Pt + CO \rightarrow Pt–CO_{ads}$) and Ru decomposes and adsorbs OH radicals from water at low potentials ($Ru + H_2O \rightarrow Ru–OH_{ads} + H^+ + e^-$), which rapidly oxidizes CO on the Pt surface to CO_2 for discharge ($Pt–CO_{ads} + Ru–OH_{ads} \rightarrow CO_2 + H^+ + e^-$), exposing the Pt active site and restoring the catalytic activity.[32] Yunteng Qu *et al.* prepared a Pt–SnO_2/graphene catalyst and tested the *i–t* curve, finding out that the resistance to CO poisoning was significantly better than Pt/graphene because the formation of adsorbed oxygen-containing groups OH_{ads} on the SnO_2 surface at low potentials could improve the efficiency of CO oxidation.[33] Xiuyu Wang *et al.* investigated that applying Pt–Au/CNT@TiO_2 catalyst prepared by adding TiO_2 to Pt–Au/CNT to the system could improve the resistance to poisoning. One reason is that TiO_2 increases the electron density of the alloy by interacting with Pt–Au alloy, and some electrons are transferred to the anti-bonding orbital of CO, weakening the bonding strength of the C–O bond while reducing the oxidation overpotential. For another, according to the bifunctional mechanism, the Ti ions in the high valence state decompose water molecules to form OH_{ads} species in the adsorbed state, which oxidize CO on the Pt surface to produce CO_2.[34] There are also Pt–RuO_2,[35,36] Pt–ZrO_2 (ref. 37 and 38) and Pt–WO_3 (ref. 39 and 40) that improve the catalyst's resistance to CO poisoning through a bifunctional mechanism. (2) By changing the electronic structure of Pt through the ligand effect, the bond strength between Pt carbonyl groups ($Pt–CO_{ads}$) could be weakened, which is conducive to promoting the oxidative desorption of CO and improving the resistance of the catalyst to poisoning. J. R. Kitchin *et al.* found through density function theory that Pt–Ti, Pt–V, Pt–Cr, Pt–Mn, Pt–Fe, Pt–Co Pt–Ni bimetals can change the electronic structure of the Pt surface through electronic interactions, also known as the ligand effect, thus changing chemical properties and weakening ability of platinum to adsorb CO.[41] (3) The introduction of oxygen-containing groups in the catalyst carrier improves the resistance to CO poisoning of the catalyst. Xiaomei Chen *et al.* prepared the catalyst PtPdNPs/GNs by loading Pt–Pd alloys on graphene nanosheets and prepared catalysts Pt/GNs, Pd/GNs, PtPdNPs/C for comparison. The 1000 second *i–t* curves were tested to evaluate the resistance of the catalysts to CO poisoning. At the end of the 1000 second test, the ethanol oxidation current density of PtPdNPs/GNs was still much higher than the other catalysts, so the resistance to CO poisoning was better. One of the reasons for the improved resistance to poisoning is that the authors used the Hummers' method to prepare graphene oxide, where the carrier introduces a large number of oxygen-containing groups, which are later reduced to graphene as the catalyst carrier, and the remaining oxygen-containing groups on the carrier help to remove CO from the Pt–Pd alloy. The other reason is that, relative to Pt, Pd is proved to be more oxytropic with lower cost, which can act as an oxidation promoter by forming oxygen-containing species on the Pd metal particles, oxidizing and removing CO from the Pt surface.[42]

The natural abundance of ^{232}Th is almost 100%, with a half-life of 1.4×10^{10} years, a thorium valence of +4 corresponding to the oxide ThO_2, insoluble in water and alkali while soluble in H_2SO_4 solution.[43] Lijin Xu *et al.*[44] mixed $SrCO_3$, $BaSO_4$ and ThO_2 powders in a mortar and crushed them into small particles under high pressure, and calcined at 900 °C for 0.5 h to obtain the catalyst. The catalyst was then utilized to catalyze the methane oxidation coupling reaction. During the action of the catalyst, the hydrocarbon bond of methane is broken and the hydrogen is released to interact with oxygen to form water, likewise the C_2 double bond (alkene bond) is formed to produce olefins. The addition of ThO_2 significantly improves the C_2 yield and C_2 selectivity relative to $SrCO_3$/$BaSO_4$, since introducing ThO_2 substitutes Th^{4+} for Sr^{2+} as well as Ba^{2+}, increasing the number of lattice defects and improving the catalytic activity. Ramya Arumugam *et al.*[45] synthesized ThO_2/Fe_3O_4 nanocomposites by hydrothermal methods with larger specific surface area, more active sites and higher stability for the catalytic and removal of triphenylmethane dyes (MG) from the aqueous phase with a degradation rate about 99.53% at pH = 5. Nanostructured N-doped ThO_2 was synthesized by Wei, HT *et al.*[46] and the material exhibited significant visible light absorption and high photocatalytic activity for the reduction of Cr(VI) under visible light (wavelength >420 nm) irradiation. Co–ThO_2–ZSM-5 bifunctional zeolite catalysts were prepared for catalyzing the conversion of carbon monoxide and hydrogen to hydrocarbons by Murty A. N. *et al.*[47] The catalytic performance (*i.e.* activity and selectivity) of the composites depended on the content of cobalt on the mesoporous zeolite ZSM-5 and the co-catalytic effect of ThO_2. Considering the co-catalytic effect of ThO_2 as shown above and the radioactivity property of it, we selected ThO_2 to inspect its effect on the Pt/C catalyst.

In this work, we report the catalytic activity, durability, and resistance to CO poisoning of the novel catalyst Pt–ThO_2/C in which the catalytic activity of ThO_2 was firstly taken into consideration to address the problem of CO poisoning in the anode Pt/C catalyst of DEFC. The catalyst Pt–ThO_2/C was synthesized by loading Pt particles onto the ThO_2-loaded carbon carrier *via* impregnation–reduction method and characterized by TEM, EDS, XRD, ICP-MS and XPS. The catalytic performance of the catalyst was tested by an electrochemical workstation and three electrodes. Likewise, Pt–*x*ThO_2/C was assembled into a fuel cell to test the maximum cell power density.

Results and discussion

Physical characterization results

TEM. Fig. 1(a) shows the TEM image and the particle distribution of the ThO_2 which reveals that ThO_2 particles prepared by hydrothermal method have good dispersion and relatively uniform particle size with an average particle size of 3.86 nm. Fig. 1(b–d) show the TEM images and the Pt particle distribution of the Pt-6.67%ThO_2/C, Pt-40%ThO_2/C and Pt/C–$NaBH_4$. As is indicated in the figure, the distribution of Pt on the carbon carrier is rather agglomerated with uneven dispersion, probably due to the violent reaction of $NaBH_4$ in reducing H_2PtCl_6. Based on the particle distribution, the average particle sizes are 11.09 nm, 14.15 nm and 12.40 nm in order in which the average particle size of the catalyst is the largest when the

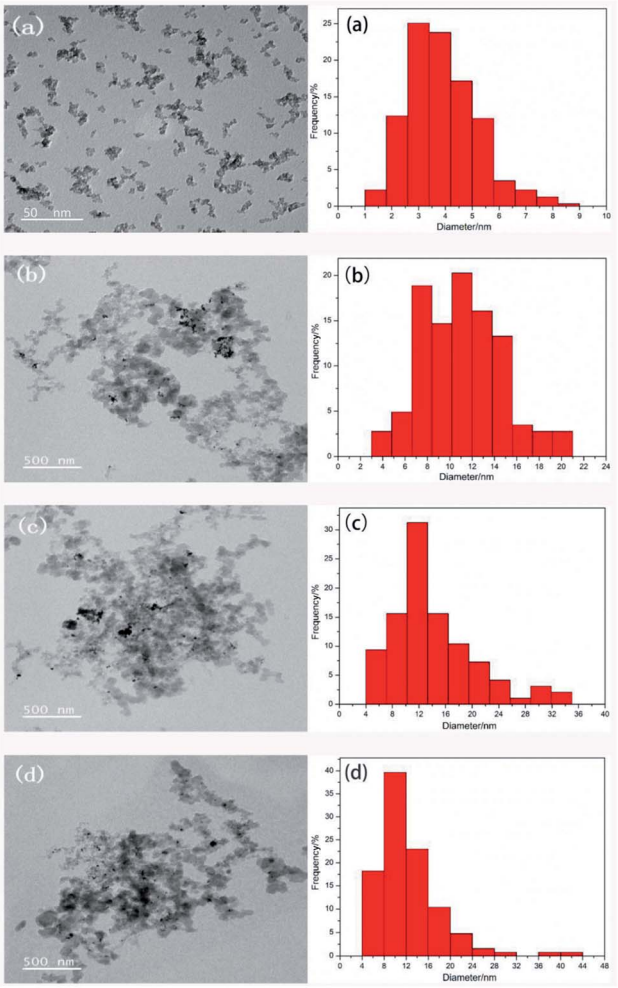

Fig. 1 (a) TEM micrograph and particle size distribution of ThO_2; TEM micrographs and the Pt particle size distribution of the synthesized catalysts (b) Pt-6.67%ThO_2/C, (c) Pt-40%ThO_2/C and (d) Pt/C–$NaBH_4$, respectively.

mass fraction of ThO_2 is 40%. Probably the increased number of particles loaded on the carbon results in poorer dispersion and increased agglomeration.

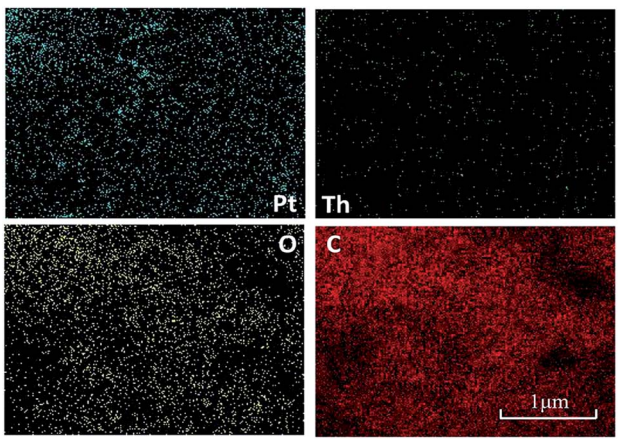

Fig. 2 Pt–ThO_2/C catalyst surface distribution of Th, Pt, C and O.

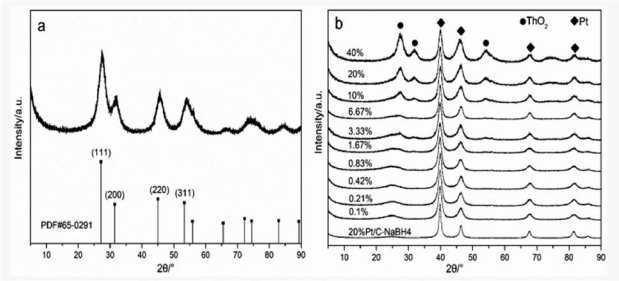

Fig. 3 X-ray diffraction patterns of (a) ThO_2 and (b) Pt–xThO_2/C.

EDS. The EDS analysis of surface distribution as shown in Fig. 2 clarified that both Pt and ThO_2 are successfully loaded on the carbon carrier. What's more, ThO_2 particles (also the ^{232}Th) are well dispersed on the catalyst.

XRD. The XRD patterns of the prepared materials are shown in Fig. 3. Fig. 3(a) is the XRD pattern of ThO_2 prepared by hydrothermal method, the peak positions and relative intensities of the diffraction peaks correspond to the ThO_2 standard PDF card 65-0291. Fig. 3(b) is the XRD pattern of the 11 catalysts, the diffraction peaks at 27° and 31° correspond to the (111) and (200) crystalline planes of ThO_2, and the diffraction peaks at 39° and 46° correspond to the (111) and (200) reflections of Pt. The XRD patterns indicate that ThO_2 and Pt have been loaded onto the carbon. As the loading of ThO_2 increases, the diffraction peaks become stronger and stronger, while the diffraction peaks of Pt basically remain the same except that the peak at 46° becomes sharper indicating the content of (200) reflection increases and the crystalline grain of Pt enlarges. The result of larger crystalline grain of Pt with increased loading of ThO_2 is also consistent with Fig. 1(b) and (c).

XPS. As shown in the Fig. 4, the presence of C, Pt, O and Th in the Pt-10 wt%ThO_2/C catalyst are confirmed. The two peak of Th

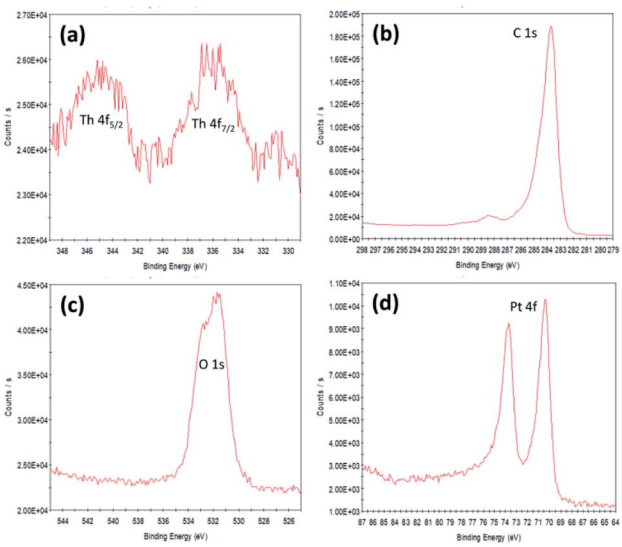

Fig. 4 XPS regions (a) Th $4f_{5/2}$ and $4f_{7/2}$, (b) C 1s, (c) O 1s and (d) Pt 4f lines of Pt-10 wt%ThO_2/C.

Table 1 Actual loading value of Pt and ThO_2 in the catalysts

Catalysts	Pt	ThO_2
20%Pt-40%ThO_2/C	18.9%	36.3%
20%Pt-20%ThO_2/C	19.0%	19.4%
20%Pt-10%ThO_2/C	19.3%	9.9%
20%Pt-6.67%ThO_2/C	18.2%	6.0%
20%Pt-3.33%ThO_2/C	20.9%	3.3%
20%Pt-1.67%ThO_2/C	19.5%	1.5%
20%Pt-0.83%ThO_2/C	19.7%	0.9%
20%Pt-0.42%ThO_2/C	19.4%	0.4%
20%Pt-0.21%ThO_2/C	18.9%	0.1%
20%Pt-0.1%ThO_2/C	19.2%	0.08%
20%Pt/C–$NaBH_4$	19.3%	0

$4f_{5/2}$ and Th $4f_{7/2}$ components assigned to Th^{4+} in ThO_2 are centered at 343.7 and 336.2 eV according to Fig. 4(a), respectively.[48,49] The C 1s line showed one peak located at 284.4 eV (Fig. 4(b)) while the O 1s line showed apparently two peaks located at 531.2 eV and 532.7 eV (Fig. 4(c)) assigned to the oxygen atoms strongly bonded to Th and the oxygen in H_2O adsorbed on the surface, respectively.[50] The peaks in the Fig. 4(d) centered at 70.2 eV and 73.8 eV are identical to Pt 4f spectra, which are assigned to Pt^0. The peaks are shifted to lower binding energy relative to Pt^0 probably owing to the donation of electrons from ThO_2 to Pt.[51]

ICP-MS. As shown in Table 1, the actual loading of Pt and ThO_2 on carbon in the catalyst is close to the theoretical values. This is due to that H_2PtCl_6 is readily reduced by $NaBH_4$ and the carbon has a strong adsorption load capacity on Pt and ThO_2 particles.

Catalytic performance for ethanol oxidation reaction (EOR)

The cyclic voltametric (CV) curves of the 8 catalysts in a mixture solution of 0.5 mol L^{-1} H_2SO_4 and 0.5 mol L^{-1} C_2H_5OH are presented in Fig. 5. By comparing the magnitudes of the ethanol oxidation peak current densities of different catalysts, it was found that the addition of ThO_2 as a catalytic additive to Pt/C could improve the catalytic activity, and the ethanol oxidation peak current density of Pt-6.67%ThO_2/C (3.38 mA cm^{-2}) was significantly higher than Pt/C–$NaBH_4$ (2.34 mA cm^{-2}), which might be due to the synergy between Pt and Th. It can also be observed that the catalytic activity of the material gradually increases as the mass fraction of ThO_2 in the catalyst increases from 0.1%. The maximum activity is achieved at a ThO_2 mass fraction of 6.67% and subsequent increases in ThO_2 content result in a significant decrease in the catalytic activity of the material. This is due to the fact that the mass fraction of Pt in the catalyst is fixed and increasing the ThO_2 content leads to a relative reduction in the carbon content and the fact that ThO_2 is non-conductive, which seriously affects the conductivity of the catalyst. On the other hand, an increase in ThO_2 content leads to an increase in the density of the particles loaded on the carbon, causing agglomeration, which can also affect the catalytic activity.

The retention rates of catalytic activity of prepared 11 catalysts after scanning 200 circles CV in a mixture solution of

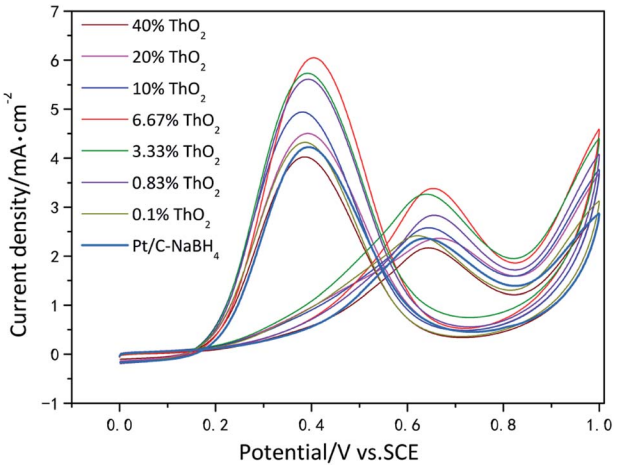

Fig. 5 Cyclic voltamograms of ethanol oxidation on catalyst systems in a mixture of 0.5 mol L^{-1} H_2SO_4 + 0.5 mol L^{-1} C_2H_5OH solution at 25 °C at a scan rate of 50 mV s^{-1}.

0.5 mol L^{-1} H_2SO_4 and 0.5 mol L^{-1} C_2H_5OH are listed in Table 2, which are used to evaluate the durability performance of the catalysts. By comparing the activity retention rate of the different catalysts on the 200th circle, it can be seen that the activity of the catalysts mostly remained above 90%, with only a few percentage points of decay. This may be due to the fact that the Pt particles prepared by the reduction of H_2PtCl_6 by $NaBH_4$ have a larger particle size and are lost less in acidic media. The catalytic activity of Pt-6.67%ThO_2/C was maintained at 95.5%, an increase compared to Pt/C–$NaBH_4$ (92.7%), indicating that the addition of ThO_2 can improve catalyst durability.

Fig. 6 presents the *i–t* curves of 11 catalysts in a mixture solution of 0.5 mol L^{-1} H_2SO_4 and 0.5 mol L^{-1} C_2H_5OH at a constant potential of 0.6 V (*vs.* SCE). Initially for a very short period of time, the intermediate product CO species from the oxidation of ethanol adsorb onto the active sites of Pt, forming a stable platinum carbonyl group that covers the active site of Pt, preventing further dissociation of ethanol and causing catalyst poisoning, which severely affects the catalytic activity and manifests itself as a sharp drop in the current curve. Afterwards, the adsorption and oxidative desorption of CO on the Pt surface gradually tends to a dynamic equilibrium due to the detoxification effect of ThO_2, and the current curve decreases to a flattening. It is obvious that the current curve decreases more slowly with time for Pt-6.67%ThO_2/C compared to the other catalysts. After 3000 s of constant voltage testing, the current density of Pt-6.67%ThO_2/C was 0.89 mA cm^{-2}, which was still significantly higher than Pt/C–$NaBH_4$ (0.41 mA cm^{-2}), indicating that the addition of ThO_2 enable the catalyst to reactivate the catalyst by itself. The reason for this is that α particles released by ^{232}Th irradiates water to produce OH radicals ($H_2O + *\alpha \rightarrow {}^{\bullet}OH + H^+ + e^-$), which rapidly removes CO_{ads} ($Pt\text{–}CO_{ads} + {}^{\bullet}OH \rightarrow Pt + CO_2 + H^+ + e^-$) and releases the active site of Pt. Thus, we call the whole process self-reactivation and the Pt–*x*ThO_2/C the self-reactivated catalyst.

Fig. 7 shows the chronopotentiometry curves of Pt-6.67% ThO_2/C and Pt/C–$NaBH_4$ in a mixture solution of 0.5 mol L^{-1}

Table 2 Ethanol oxidation peak current density of the 200th CV of the catalyst systems in a mixture of 0.5 mol L^{-1} H_2SO_4 + 0.5 mol L^{-1} C_2H_5OH solution at 25 °C at a scan rate of 50 mV s^{-1}

Catalysts	1st ethanol oxidation peak current density mA cm^{-2}	200th ethanol oxidation peak current density mA cm^{-2}
20%Pt-40%ThO_2/C	2.16 (100%)	1.88 (87.0%)
20%Pt-20%ThO_2/C	2.36 (100%)	2.12 (89.8%)
20%Pt-10%ThO_2/C	2.57 (100%)	2.34 (91.0%)
20%Pt-6.67%ThO_2/C	3.38 (100%)	3.23 (95.5%)
20%Pt-3.33%ThO_2/C	3.25 (100%)	3.09 (95.0%)
20%Pt-1.67%ThO_2/C	3.19 (100%)	3.11 (97.4%)
20%Pt-0.83%ThO_2/C	2.82 (100%)	2.74 (97.1%)
20%Pt-0.42%ThO_2/C	3.01 (100%)	2.94 (97.6%)
20%Pt-0.21%ThO_2/C	2.64 (100%)	2.58 (97.7%)
20%Pt-0.1%ThO_2/C	2.40 (100%)	2.29 (95.4%)
20%Pt/C–$NaBH_4$	2.34 (100%)	2.17 (92.7%)

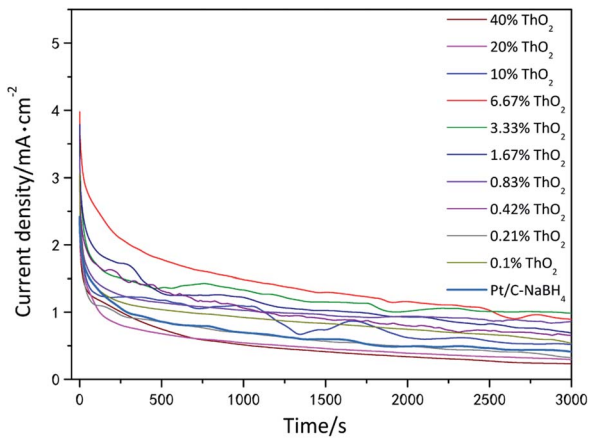

Fig. 6 Amperometric *i–t* curves of ethanol oxidation on catalyst systems in a mixture of 0.5 mol L^{-1} H_2SO_4 + 0.5 mol L^{-1} C_2H_5OH solution at 25 °C at 0.6 V (*vs.* SCE) for 3000 s.

H_2SO_4 and 0.5 mol L^{-1} C_2H_5OH at a constant current of 0.1 mA. Within a very short initial period of time, the electrode potential rises sharply to the ethanol oxidation onset potential. As the test time increases, the electrode potential first rises slowly. The intermediate product CO produced during the oxidation of ethanol gradually accumulates on the catalyst surface, making the electrocatalytic activity of the catalyst decrease and the overpotential of ethanol oxidation increase, and in order to meet the set current conditions, the electrode potential must rise accordingly. As the catalyst is further poisoned, the catalyst surface is almost completely covered with toxic species and the electrocatalytic oxidation of ethanol is almost impossible, at which point the electrode potential rises sharply until it reaches the oxygen precipitation potential as a means of meeting the set current demand. The resistance of the catalyst to CO poisoning is evaluated on the basis of the time taken for the electrode potential to rise sharply to a sudden jump in potential. Pt-6.67% ThO_2/C shows a potential jump time of 337 s and Pt/C–$NaBH_4$ shows a potential jump time of 60 s, so Pt-6.67%ThO_2/C is more resistant to CO poisoning, most likely due to the self-reactivation effect mentioned above.

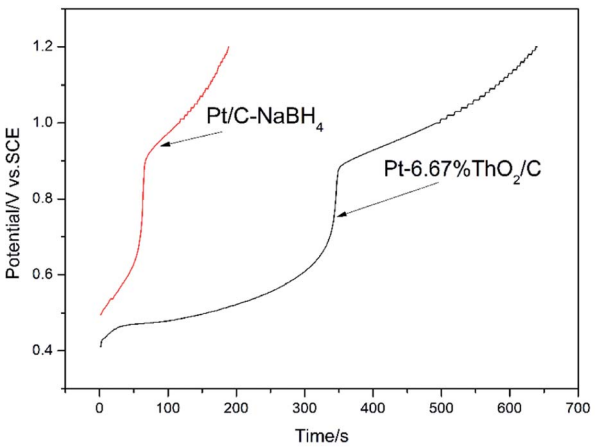

Fig. 7 Chronopotentiometry curves of ethanol oxidation on catalyst systems in a mixture of 0.5 mol L^{-1} H_2SO_4 and 0.5 mol L^{-1} C_2H_5OH solution at 25 °C at 0.1 mA.

Single cell performance

To further investigate the modification effect of ThO_2 on Pt/C catalyst, Pt-6.67%ThO_2/C and Pt/C–$NaBH_4$ were used as anode catalyst to assemble single cell and respectively test the cell *V–i* polarization curves. Fig. 8 shows the *V–i* polarization curves and power density curves for the two catalysts. The *V–i* curve is polarized for three main reasons, one is activation polarization, when a chemical reaction occurs on the electrode surface to output current, the reaction resistance must be overcome, the reaction resistance leads to polarization. Secondly, ohmic polarization, when the battery is operated, the flow of ions and electrons will be subject to resistance to produce a voltage drop, and resistance leads to polarization. Third is the concentration difference polarization, if the rate of transport of ethanol to the electrode is less than the rate of consumption, it will cause the concentration of ethanol on the surface of the electrode to be lower than its own concentration, this concentration difference leads to polarization.

Fig. 8 *V–i* curves also show that the polarization of Pt/C–$NaBH_4$ is more obviously than Pt-6.67%ThO_2/C. Moreover, according to the power density curves, it can be found that the

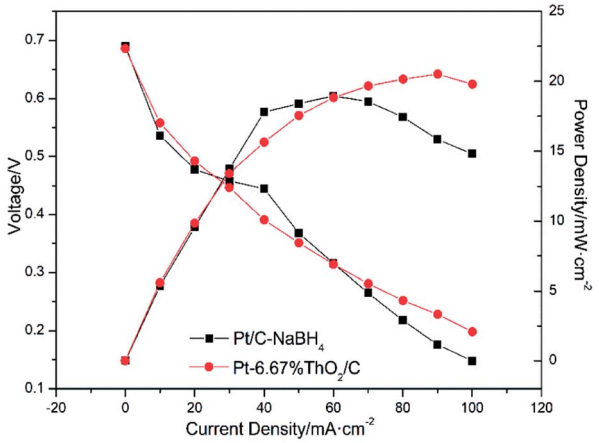

Fig. 8 Cell voltage and power density as a function of current density for the single cell with Pt-6.67%ThO_2/C catalyst (anode) and Pt/C–$NaBH_4$ catalyst (anode) operating at 60 °C.

maximum power density of single cell is 20.52 mW cm^{-2} for Pt-6.67%ThO_2/C and 18.96 mW cm^{-2} for Pt/C–$NaBH_4$. So it is further clear from the fuel cell test results that the addition of ThO_2 can improve Pt/C catalytic performance.

Experimental

Materials

Cabot carbon (XC-72) was purchased from Suzhou Sinero. $Th(NO_3)_4 \cdot 4H_2O$ (AR) was purchased from Changsha Jingkang. $H_2PtCl_6 \cdot 6H_2O$ (AR), $Na_3C_6H_5O_7 \cdot 2H_2O$ (AR), C_2H_5OH (GR), $NaBH_4$ (AR) were purchased from Aladdin reagent. NaOH (AR) and H_2SO_4 (AR) were purchased from sinopharm chemical reagent. C_3H_8O (AR) was purchased from Macklin reagent. Nafion (5 wt%) was purchased from Shanghai Hesen.

Synthesis of Pt–ThO_2/C catalysts

Procedure for synthesis of ThO_2. 5 mL of 0.8 mol L^{-1} $Th(NO_3)_4 \cdot 4H_2O$ solution was added dropwise to 75 mL of 6.4 mol L^{-1} NaOH (aq) and the mixed solution was stirred at room temperature for 30 min. The mixed solution was then transferred into a 100 mL Teflon lined stainless steel reactor with hydrothermal treatment at 100 °C for 24 h. After the reactor had cooled to room temperature, the material was washed with ultrapure water and dried to obtain the white powder of ThO_2.

Procedure for synthesis of Pt–$x$$ThO_2$/C catalysts. Weigh 146 mg of carbon into a round bottom flask, add 50 mL of ultrapure water and 25 mL of C_3H_8O into the flask, sonicate for 20 min, stir for 10 min, then adjust the solution pH > 10 with 0.1 mol L^{-1} NaOH. 14 mg of homemade ThO_2 was added into 5 mL of ultrapure water, sonicate and disperse, then pour into the flask and stir for 10 min. Subsequently, a solution of $H_2PtCl_6 \cdot 6H_2O$ containing 42 mg Pt and 13 mg $Na_3C_6H_5O_7 \cdot 2H_2O$ were added in the flask. After stirring for 20 min the flask was transferred to a water bath at 80 °C and stirred for 2 h, during which time an excess of $NaBH_4$ solution was added dropwise to the flask. Finally, the material was washed by centrifugation using ultrapure water, dried overnight at 60 °C and ground to obtain the catalyst, noted as Pt-6.67%ThO_2/C. Note that the percentages mentioned about ThO_2 are all mass fraction in this article. The same process was used to prepare other Pt–$x$$ThO_2$/C ($x$ = 40, 20, 10, 3.33, 1.67, 0.83, 0.42, 0.21 and 0.1%) as well as Pt/C–$NaBH_4$ with a stable Pt loading of 20 wt% in all catalysts.

Physical characterizations

The microstructure of Pt–$x$$ThO_2$/C Pt–$x$$ThO_2$/C and Pt/C–$NaBH_4$ was observed by the transmission electron microscopy (TEM) measurement with JEM-F200 manufactured by Japan Electronics Corporation. The sample was prepared by sonicating the material into anhydrous ethanol and then adding a small amount of the suspension drop by drop onto a copper grid to dry for measurement.

Energy dispersive spectroscopy (EDS) tests were carried up on a SU8020 manufactured in Hitachi of Japan to roughly observe the existence and distribution of the elements on the surface of the catalyst Pt–$x$$ThO_2$/C.

The physical phases present in the material was characterized by the X-ray diffraction technique (XRD) on a Bruker D8 ADVANCE, manufactured in Germany, equipped with a Cu-Kα X-ray source and operated at a voltage of 40 kV, a current of 40 mA and a test angle of 5–90°.

The X-ray photoelectron spectroscopy (XPS) was obtained on a VG Multilab 2000 using Al Kα (1486.7 eV) as the exciting radiation to further confirm the presence and the chemical states of the elements at the materials' surface.

Inductively coupled plasma mass spectrometer (ICP-MS) measurements were conducted on an Agilent 7850 ICP-MS from Agilen of Japan to analyze the elemental content of the solution.

Electrochemical measurements

An electrochemical workstation with a three-electrode system was used to test the catalytic performance of the catalysts. The electrochemical workstation used for the experiments was manufactured by Shanghai Chenhua, model CHI760E. The three electrodes are, in order, a saturated calomel electrode as reference electrode, model CHI150, with a saturated KCl solution inside the saturated calomel electrode; a platinum wire electrode as counter electrode, model CHI115; and a glassy carbon electrode as working electrode, model CHI104, with a 3 mm diameter glassy carbon in the middle part of the glassy carbon electrode. All three electrodes were purchased from Shanghai Chenhua. When the electrochemical workstation is in operation, the three electrodes form two circuits, where the working electrode loaded with catalyst and the reference electrode form a circuit to test the working electrode potential, as the reference electrode potential is known to be constant. For example, the standard electrode potential of a saturated calomel electrode is 0.2412 V. The potential output from the workstation is the difference in potential between the working and reference electrodes. The working electrode and counter electrode form a circuit to test the working electrode current, this is known as the "three electrodes and two circuits". The

working electrode is prepared as follows: using in turn 0.3 μm and 0.05 μm Al_2O_3 powder, the electrode is polished on a polishing flannel with the aim of polishing the glassy carbon to a mirror-like surface without scratches and the PTFE material wrapped around the glassy carbon to a very hydrophobic surface. Weigh 10 mg of the catalyst to be tested, add to 2.4 mL of ultra-pure water, 0.1 mL of Nafion, 2.5 mL of C_3H_8O and sonicate for 30 min to obtain a 2 mg mL^{-1} slurry of catalyst. Pipette 5 μL of the slurry onto the glassy carbon electrode and allow drying naturally as a working electrode.

Fuel cell measurements

The catalyst to be tested was ultrasonically dispersed with the Nafion solution in C_3H_8O under ice bath conditions. The catalyst suspension was then sprayed onto a PTFE film as the catalytic layer and subsequently hot-pressed onto both sides of a Nafion 115 film at 120 °C and 10 MPa maintained for 120 s. The outermost side used carbon cloth (H2315T10AC1 NOK, Japan) as the diffusion layer to form a membrane electrode (MEA) with an effective area of 2 × 2.5 cm^2. A homemade catalyst with a Pt loading of 1.2 mg cm^{-2} was used for the cell anode and a commercial Pt/C with a Pt loading of 1.2 mg cm^{-2} was used for the cathode, with a Nafion solution (5 wt%) content of 15 wt% for the anode and 10 wt% for the cathode. The cell operating temperature was set at 60 °C with 2 mol L^{-1} C_2H_5OH passing through the anode at a flow rate of 1.5 sccm and O_2 passing through the cathode at a flow rate of 400 sccm. Prior to testing, a 0.5 mol L^{-1} H_2SO_4 solution was passed from the anode for 30 min at 55 °C for reducing the internal resistance of the proton exchange membrane. The test was then started after passing 0.5 sccm of 1.5 mol L^{-1} C_2H_5OH solution on the anode side and 800 sccm of O_2 on the cathode and discharging at 100 mA cm^{-2} for 10 hours for stabilizing the internal mass transfer channels of the catalytic layer.

Conclusions

To settle the low activity and susceptibility to CO poisoning of Pt/C anode catalysts for DEFC, a radioactive ThO_2 catalytic additive prepared by hydrothermal method was introduced into the Pt/C catalyst at first time. TEM, EDS, XRD, XPS and ICP-MS characterization revealed that Pt and ThO_2 were successfully loaded on the carbon carrier and evenly distributed, while the Pt particles were poorly dispersed on the carbon and showed significant agglomeration due to the relatively rapid and violent reaction of $NaBH_4$ in reducing H_2PtCl_6.

The catalyst performance was determined by electrochemical workstation equipped with three electrodes. It was illustrated by the results that the catalysts prepared with 20% mass fraction of Pt and 6.67% mass fraction of ThO_2 showed the best catalytic activity and resistance to CO poisoning which was significantly improved the performance compared to Pt/C–$NaBH_4$. The increases mentioned above are partly due to the synergistic effect of Pt and Th. Moreover, Pt–$x$$ThO_2$/C is a self-reactivated catalyst, *i.e.*, α particles released by the radioactive ^{232}Th irradiate water to produce a large amount of strongly oxidizing hydroxyl radicals, which oxidize the CO adsorbed on Pt surface, expose the active site of Pt and promote further dissociation of ethanol. The results of the single cell operating performance of Pt-6.67%ThO_2/C and Pt/C–$NaBH_4$ used as anode catalysts in DEFC respectively illustrated that the cell polarization was much more severe for Pt/C–$NaBH_4$, and the maximum power density of the cell was higher for Pt-6.67% ThO_2/C than that of Pt/C–$NaBH_4$, further confirming the impressive self-reactivation effect of ThO_2 on Pt/C catalyst.

Author contributions

Yubing Xue: formal analysis, investigation, visualization, writing – original draft. Dashu Pan: formal analysis, validation. Feng Zuo: data curation, investigation. Songtao Xiao: methodology, project administration. Xiang Li: formal analysis. Fuyan Lou: resources. Mingming Li: writing – review&editing. Yinggen Ouyang: funding acquisition, conceptualization, supervision.

Conflicts of interest

There are no conflicts to declare.

Acknowledgements

The authors gratefully acknowledge the financial support for this project provided by the National Natural Science Foundation of China.

Notes and references

1 H. Zeng and H. Li, *IOP Conf. Ser.: Earth Environ. Sci*, 2020, **440**, 042010.
2 X. Xu, Z. Wei, Q. Ji, C. Wang and G. Gao, *Resour. Policy*, 2019, **63**, 101470.
3 J. Seweryn and A. Lewera, *Appl. Catal., B*, 2014, **144**, 129–134.
4 J. R. C. Salgado, V. A. Paganin, E. R. Gonzalez, M. F. Montemor, I. Tacchini, A. Anson, M. A. Salvador, P. Ferreira, F. M. L. Figueiredo and M. G. S. Ferreira, *Int. J. Hydrogen Energy*, 2013, **38**, 910–920.
5 V. Livshits, M. Philosoph and E. Peled, *J. Power Sources*, 2008, **178**, 687–691.
6 A. Anis, S. Al-Zahrani and F. A. El Aleem, *Int. J. Electrochem. Sci.*, 2012, **7**, 6221–6233.
7 V. K. Puthiyapura, D. J. L. Brett, A. E. Russell, W. Lin and C. Hardacre, *ACS Appl. Mater. Interfaces*, 2016, **8**, 12859–12870.
8 U. Lucia, *Renewable Sustainable Energy Rev.*, 2014, **30**, 164–169.
9 O. Z. Sharaf and M. F. Orhan, *Renewable Sustainable Energy Rev.*, 2014, **32**, 810–853.
10 T. Maiyalagan and S. Pasupathi, *Mater. Sci. Forum*, 2010, **657**, 143–189.
11 D. M. Fadzillah, S. K. Kamarudin, M. A. Zainoodin and M. S. Masdar, *Int. J. Hydrogen Energy*, 2019, **44**, 3031–3054.
12 S. P. S. Badwal, S. Giddey, A. Kulkarni, J. Goel and S. Basu, *Appl. Energy*, 2015, **145**, 80–103.

13 A. Serov and C. Kwak, *Appl. Catal., B*, 2010, **97**, 1–12.
14 S. Song, W. Zhou, Z. Liang, R. Cai, G. Sun, Q. Xin, V. Stergiopoulos and P. Tsiakaras, *Appl. Catal., B*, 2005, **55**, 65–72.
15 S. Samad, K. S. Loh, W. Y. Wong, T. K. Lee, J. Sunarso, S. T. Chong and W. R. W. Daud, *Int. J. Hydrogen Energy*, 2018, **43**, 7823–7854.
16 M. Ercelik, A. Ozden, Y. Devrim and C. O. Colpan, *Int. J. Hydrogen Energy*, 2017, **42**, 2658–2668.
17 Y. Devrim, S. Erkan, N. Bac and I. Eroglu, *Int. J. Energy Res.*, 2012, **37**, 435–442.
18 B. Fang, L. Daniel, A. Bonakdarpour and D. P. Wilkinson, *Adv. Mater. Interfaces*, 2022, 2200349.
19 G. Liu, Z. Yang, X. Wang and B. Fang, *Nanomaterials*, 2021, **11**, 3462.
20 A. Nouri-Khorasani, A. Bonakdarpour, B. Fang and D. P. Wilkinson, *ACS Appl. Mater. Interfaces*, 2022, **14**, 9084–9096.
21 B. Fang, L. Daniel, A. Bonakdarpour, R. Govindarajan, J. Sharman and D. P. Wilkinson, *Small*, 2021, **17**, 2102288.
22 M. S. Kim, B. Fang, N. K. Chaudhari, M. Song, T. S. Bae and J. S. Yu, *Electrochim. Acta*, 2010, **55**, 4543–4550.
23 L. Lu, B. Wang, D. Wu, S. Zou and B. Fang, *Nanoscale*, 2021, **13**, 3709–3722.
24 L. Lu, S. Zou and B. Fang, *ACS Catal.*, 2021, **11**, 6020–6058.
25 V. B. Oliveira, J. P. Pereira and A. M. F. R. Pinto, *Energy*, 2017, **133**, 652–665.
26 M. A. F. Akhairi and S. K. Kamarudin, *Int. J. Hydrogen Energy*, 2016, **41**, 4214–4228.
27 K. Miyazaki, T. Matsumiya, T. Abe, H. Kurata, T. Fukutsuka, K. Kojima and Z. Ogumi, *Electrochim. Acta*, 2011, **56**, 7610–7614.
28 Z. Zakaria, S. K. Kamarudin and S. N. Timmiati, *Appl. Energy*, 2016, **163**, 334–342.
29 A. Arshad, H. Ali, A. Habib and M. A. Bashir, *Therm. Sci. Eng. Prog.*, 2019, **9**, 308–321.
30 R. Ali and A. Pasha, *IOP Conf. Ser.: Mater. Sci. Eng.*, 2018, **376**, 012103.
31 K. A. Page and B. W. Rowe, *Polymers for Energy Storage and Delivery: Polyelectrolytes for Batteries and Fuel Cells*, 2012, 1096, pp. 147–164.
32 M. Watanabe and S. Motoo, *J. Electroanal. Chem. Interfacial Electrochem.*, 1975, **60**, 275–283.
33 Y. Qu, Y. Gao, L. Wang, J. Rao and G. Yin, *Chemistry*, 2016, **22**, 193–198.
34 X. Wang, J. Zhang and H. Zhu, *Chin. J. Catal.*, 2011, **32**, 74–79.
35 Y. Gu and W. Wong, *J. Electrochem. Soc.*, 2006, **153**, A1714–A1718.
36 Z. Chen, X. Qiu, B. Lu, S. Zhang, W. Zhu and L. Chen, *Electrochem. Commun.*, 2005, **7**, 593–596.
37 Y. Bai, J. Wu, J. Xi, J. Wang, W. Zhu, L. Chen and X. Qiu, *Electrochem. Commun.*, 2005, **7**, 1087–1090.
38 H. Song, X. Qiu and F. Li, *Appl. Catal., A*, 2009, **364**, 1–7.
39 V. Raghuveer and B. Viswanathan, *J. Power Sources*, 2005, **144**, 1–10.
40 D. Zhang, Z. Ma, G. Wang, K. Kongstantinov, X. Yuan and H. Liu, *Electrochem. Solid-State Lett.*, 2006, **9**, A423–A426.
41 J. R. Kitchin, J. K. Norskov, M. A. Barteau and J. G. Chen, *J. Chem. Phys.*, 2004, **120**, 10240–10246.
42 X. Chen, Z. Cai, X. Chen X and M. Oyama, *J. Mater. Chem. A*, 2014, **2**, 315–320.
43 A. H. Alomari, M. A. Saleh, S. Hashim, A. Alsayaheen, I. Abdeldin and A. Abukashabeh, *Radiat. Phys. Chem.*, 2020, **170**, 108660.
44 X. Lijin, Q. Fali and L. Shaoje, *J. Nat. Gas Chem.*, 1996, **5**, 136.
45 R. Arumugam, P. Periakaruppan and R. Selvanathan, *Int. J. Pharm. Sci. Res.*, 2019, **10**, 2902–2910.
46 H. T. Wei, Y. T. Wen and Y. C. Zhang, *Catal. Commun.*, 2017, **99**, 66–70.
47 A. N. Murty, A. A. Williams, R. T. Obermyer and V. U. S. Rao, *J. Appl. Phys.*, 1987, **61**, 4361–4363.
48 A. C. Ferreira, A. P. Goncalves, T. A. Gasche, A. M. Ferraria, A. M. Botelho do Rego, M. R. Correia, A. M. Bola and J. B. Branco, *J. Alloys Compd.*, 2010, **497**, 249–258.
49 F. J. Pereira, M. A. Castro, M. D. Vázquez, L. Debán and A. J. Aller, *J. Lumin.*, 2017, **184**, 169–178.
50 Y. Huentupil, G. Cabello-Guzmán, B. Chornich, R. Arancibia and G. E. Buono-Core, *Polyhedron*, 2019, **157**, 225–231.
51 H. Iida and A. Igarashi, *Appl. Catal., A*, 2006, **298**, 152–160.